High-Speed *in Situ* X-ray Scattering of Carbon Nanotube Film Nucleation and Self-Organization

Eric R. Meshot,[†,#] Eric Verploegen,[‡,§] Mostafa Bedewy,[†] Sameh Tawfick,[†] Arthur R. Woll,[⊥] Katherine S. Green,[∥] Marianne Hromalik,[∥,△] Lucas J. Koerner,[∥,▽] Hugh T. Philipp,[∥] Mark W. Tate,[∥] Sol M. Gruner,[⊥,∥] and A. John Hart[†,*]

[†]Mechanosynthesis Group, Department of Mechanical Engineering, University of Michigan, 2350 Hayward Street, Ann Arbor, Michigan 48109, United States, [‡]Stanford Synchrotron Radiation Lightsource, SLAC National Accelerator Laboratory, 2575 Sand Hill Road, Menlo Park, California 94025, United States, [§]Department of Chemical Engineering, Stanford University, Stanford, California 94305, United States, [⊥]Cornell High Energy Synchrotron Source (CHESS), Cornell University, Route 366 & Pine Tree Road, Ithaca, New York 14853, United States, and [∥]Laboratory of Atomic and Solid State Physics, Department of Physics, Cornell University, Ithaca, New York 14853, United States. [#]Present address: IMEC, Kapeldreef 75, 3001 Heverlee, Belgium. [△]Present address: Computer Science Department, State University of New York at Oswego, Oswego, New York 13126-3599, USA. [▽]Present address: The Johns Hopkins University Applied Physics Laboratory, 11100 Johns Hopkins Road, Laurel, Maryland 20723, USA.

ABSTRACT

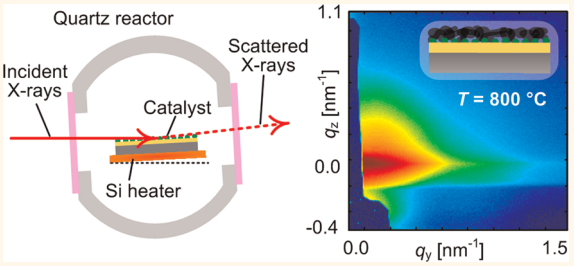

The production of high-performance carbon nanotube (CNT) materials demands understanding of the growth behavior of individual CNTs as well as collective effects among CNTs. We demonstrate the first use of grazing incidence small-angle X-ray scattering to monitor in real time the synthesis of CNT films by chemical vapor deposition. We use a custom-built cold-wall reactor along with a high-speed pixel array detector resulting in a time resolution of 10 msec. Quantitative models applied to time-resolved X-ray scattering patterns reveal that the Fe catalyst film first rapidly dewets into well-defined hemispherical particles during heating in a reducing atmosphere, and then the particles coarsen slowly upon continued annealing. After introduction of the carbon source, the initial CNT diameter distribution closely matches that of the catalyst particles. However, significant changes in CNT diameter can occur quickly during the subsequent CNT self-organization process. Correlation of time-resolved orientation data to X-ray scattering intensity and height kinetics suggests that the rate of self-organization is driven by both the CNT growth rate and density, and vertical CNT growth begins abruptly when CNT alignment reaches a critical threshold. The dynamics of CNT size evolution and self-organization vary according to the catalyst annealing conditions and substrate temperature. Knowledge of these intrinsically rapid processes is vital to improve control of CNT structure and to enable efficient manufacturing of high-density arrays of long, straight CNTs.

KEYWORDS: carbon nanotube · particle · catalyst · dewetting · X-ray scattering · kinetics · self-organization · chemical vapor deposition

Assemblies of carbon nanotubes (CNTs), including tangled films, vertically aligned "forests", and long fibers, are well-known to be attractive components of high-performance electrical interconnects,[1−5] transparent conductors,[6] light emitters,[7−9] thermal interface materials,[10,11] gas and liquid filters,[12,13] structural composites,[14,15] and photonic crystals.[16,17] For both tangled and aligned CNT films, it has been shown that properties are dominated by the organization of the CNTs rather than the properties of the individual CNTs themselves.[18−20] As a result, the functional properties of ensembles of CNTs have largely fallen short of the exceptional properties of individual CNTs. Thus, efficient manufacturing of CNT materials is a hierarchical problem, involving optimization of both individual CNT growth conditions and their collective effects.[21−23]

The dynamics of catalyst formation and subsequent CNT nucleation and growth have profound effects on the final material properties, especially in the synthesis of CNT forests, where CNT growth and self-assembly occur in concert. Although *ex situ* characterization studies have led to many important insights about the complex morphology and growth kinetics of CNT forests,[21,24−31] dynamics of the nucleation and self-organization process can only be revealed by *in situ* methods. Researchers have previously applied *in situ* methods to study CNT synthesis, such as absorption spectroscopy,[32] environmental TEM,[33−36] XPS,[36−38] and Raman spectroscopy.[39] However, many of these require low pressures that are not typical for chemical vapor deposition (CVD) of CNTs and/or do not provide quantitative information (*e.g.*, about size, shape, order) for statistically significant numbers of structures (*i.e.*, catalyst nanoparticles or CNTs). AFM and TEM are typical methods for directly imaging and measuring particles. However, their incompatibility with the high temperatures (500−900 °C) used during synthesis limits their use to

* Address correspondence to ajohnh@umich.edu.

Received for review February 20, 2012 and accepted May 9, 2012.

Published online May 09, 2012
10.1021/nn300758f

ex situ observations or requires special sample preparation and restricted operating conditions. Further, the morphology and chemistry of the catalyst may be altered during CNT growth or cooling, so *ex situ* imaging and scattering techniques may not provide an accurate interpretation of the growth process.

Previous studies have established that *in situ* small-angle X-ray scattering (SAXS) along with quantitative models can be applied to measure populations of nanostructures.[40] For example, *in situ* SAXS has been used to probe the growth of substrate-bound nanoparticles[41−43] and nanoparticles in solution[44,45] as well as the pyrolytic formation of soot.[46−48] In this paper, we present findings from the first use of grazing incidence small-angle X-ray scattering (GISAXS) to monitor CNT film growth in real time. Combining synchrotron radiation and the use of a high-speed pixel array detector, we resolve (1) the dynamics of catalyst particle formation from a metal thin film, (2) the evolution of catalyst morphology during annealing, (3) the nucleation of CNTs, and (4) the self-organization of CNTs into a vertically aligned forest. This nondestructive method interrogates statistically significant populations of nanostructures (10^9) during thermal processing over a wide temperature range, at atmospheric pressure, and at a time resolution of 10 ms.

RESULTS AND DISCUSSION

Experimental Technique. To enable this study, a custom-built, cold-wall CVD reactor is mounted in a synchrotron beamline and configured such that the X-ray beam passes over the heated substrate (Figure 1). Resistive heating of a Si platform enables localized and rapid control of the substrate (catalyst) temperature.[49,50] Thin polyimide (Kapton) windows that are highly X-ray transmissive (Figure 1b) allow incident and scattered X-rays to pass through the sealed reactor with minimal parasitic scattering.[51] An X-ray energy of 10 ± 0.1 keV is selected with synthetic multilayer optics (W/B4C, 27.1 Å *d*-spacing), and we use a 2-D pixel array detector[52,53] for X-ray imaging at a frame rate of 100 Hz. The incident collimated X-ray beam has a height of 100 μm as controlled by slits upstream of the CVD reactor. The substrate is tilted toward the X-ray beam at an angle of incidence $\alpha_i = 0.15°$, which is below the critical angle for total external reflection from the Si substrate.[54] Operating this reactor at atmospheric pressure, we study the synthesis of CNT forests from C_2H_4/H_2 precursors, which are first passed through a "pre-heater" (~1050−1070 °C) upstream of the reactor in order to thermally generate the suite of gas compounds necessary to achieve accelerated CNT growth to millimeter film thicknesses.[55,56] All experiments shown here use a bilayer thin-film catalyst, 1 nm Fe film on top of a 10 nm Al_2O_3 support, which is sequentially deposited by electron-beam evaporation onto 300 nm of thermally grown SiO_2 on (100) Si wafers.[57]

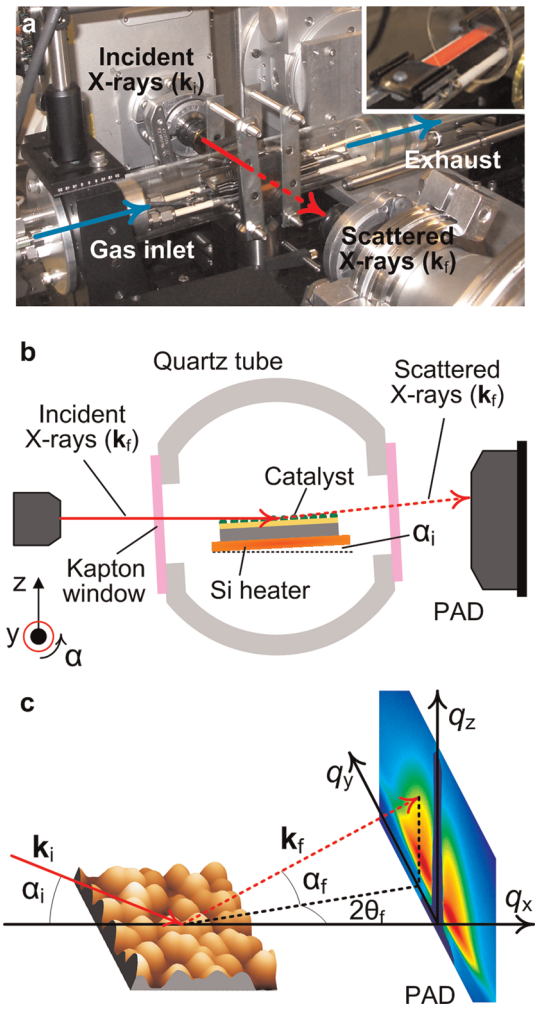

Figure 1. (a) Cold-wall CVD apparatus mounted in the path of the X-ray beam (illustrated by red arrow) on a 4-axis (*x*-*y*-*z*-α) stage in the G1 station at CHESS. The quartz tube is modified with kapton windows, and the inset image shows the heated Si platform. (b and c) Cross-section geometry of the reactor, where the sample is positioned at an angle α_i with respect to the incoming X-ray beam (k_i), and scattered X-rays (k_f) at an exit angle α_f are collected by a 2-D pixel array detector (PAD).

Distinct stages of the synthesis process for CNT forests are schematically represented in Figure 2, along with corresponding *in situ* GISAXS images. This figure provides an overview of the dynamics and their relationship to the scattering patterns, and a more in-depth discussion of the dynamics follows later. The plots beneath each image show 1-D intensity profiles *versus* the inverse space parameter $I(q_y)$, which are extracted from the 2-D images and used for fitting of the mathematical scattering models described later. The GISAXS patterns are vertically symmetric about the X-ray beam because the form factor of the particles, CNTs, and their organization in the *x*−*y* plane (substrate) are all isotropic; therefore, only one-half of the GISAXS image is required for analysis. We hereafter refer to q_y as q because we only consider this parallel scattering in this work.

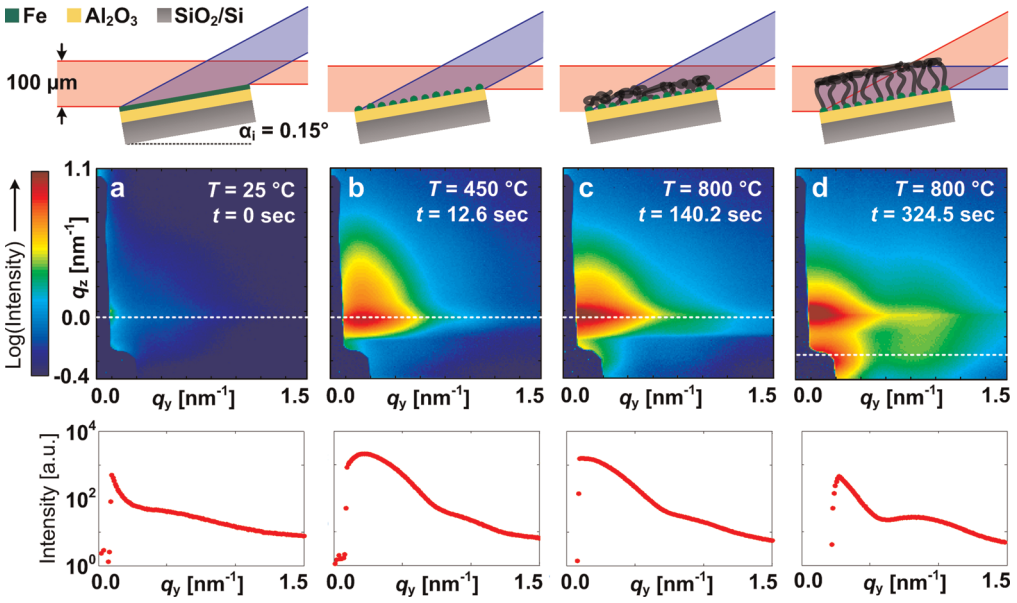

Figure 2. GISAXS images of four different stages of the CNT synthesis process: (a) as-deposited Fe/Al_2O_3 film before heating; (b) dewetting during rapid heating (Fe particles); (c) nucleation of CNTs (CNTs and Fe particles); and (d) CNT growth (only CNTs observed with transmitted beam). Each 2-D SAXS image corresponds to the schematic of scattering geometry above and the plot of $I(q_y)$ along the dashed line in the SAXS image. According to the top row schematics, the blue-shaded portion of the scattered X-ray beam is used for analysis. For example in (d), the transmitted beam corresponds to the white dashed line at a lower position on the detector compared to when the grazing incidence scattering is analyzed.

First, the substrate is annealed in H_2/He by rapidly heating to 800 °C and holding at this temperature for 2 min. It is well-known that this step causes the Fe film to reduce[36] and dewet to yield particles,[55] which determines CNT diameter.[55,58,59] However, to understand the dynamics of dewetting, it is necessary to observe the process in real time. During heating, we observe a distinct and rapid transition from diffuse scattering from the as-deposited Fe/Al_2O_3 film (Figure 2a) to coherent scattering from well-defined particles (Figure 2b), indicating that dewetting occurs over a short time frame. After the film dewets, the scattering pattern remains constant as the temperature is held, indicating that the particles do not undergo measurable coarsening during the 2 min time frame. This is discussed quantitatively later.

Next, C_2H_4 is introduced to initiate CNT nucleation and growth. Before detecting scattered X-rays from the transmission beam, we observe changes in the GISAXS pattern and a significant increase in the total scattered intensity (Figure 2c), which we attribute to the deposition of carbon at the substrate-bound nanoparticles. During the time delay (18 s) between when C_2H_4 is added and the onset of CNT scattering, the concentration of hydrocarbon is transient and surpasses a critical (albeit not precisely known) partial pressure for CNT nucleation. By real-time monitoring using a quadrupole mass spectrometer, we estimate the partial pressure of C_2H_4 is approximately 0.01 atm after 18 s, and it takes ~100 s for the C_2H_4 concentration to reach 90% of its steady state value of 0.2 atm (Supporting Information, Figure S1). When the partial pressure of C_2H_4 is 0.01−0.05 atm, the CNTs self-organize and vertical growth is detected (Figure 6). It is not surprising that nucleation occurs before the steady-state partial pressure of C_2H_4 is reached because we have previously shown that only trace amounts (0.01 atm) of active alkyne precursors (in concert with C_2H_4) can induce efficient CNT growth.[60]

Once CNTs begin growing, the specular beam contains scattering information for both Fe particles and CNTs; therefore, to monitor CNT growth we use a q_z value corresponding to the transmitted beam, which includes only scattering from CNTs (Figure 2d). For a 100 μm X-ray beam impinging at $\alpha_i = 0.15°$ on the bare 1 × 1 cm catalyst substrate (before CNT growth), we estimate that 75 μm of the beam passes over the downstream edge of the substrate without scattering. This portion of the beam is entirely blocked by the beamstop (a lead foil) and is not visible on the detector until the height of the CNT forest increases such that it scatters these X-rays onto a visible area of the detector below the GISAXS features. We use this transmission scattering to monitor and quantify prolonged, vertically aligned CNT growth. *In situ* X-ray scattering videos of both Fe particle formation and CNT nucleation are provided in the Supporting Information.

GISAXS Modeling of Catalyst Nanoparticle Arrays. We obtain quantitative measures of the particle size and spacing on the substrate by fitting the GISAXS data with a mathematical model. We adapt the approach of Renaud and co-workers[40] to model the scattering cross section of an arrangement of truncated spheres (particles) on a flat substrate (schematic model in

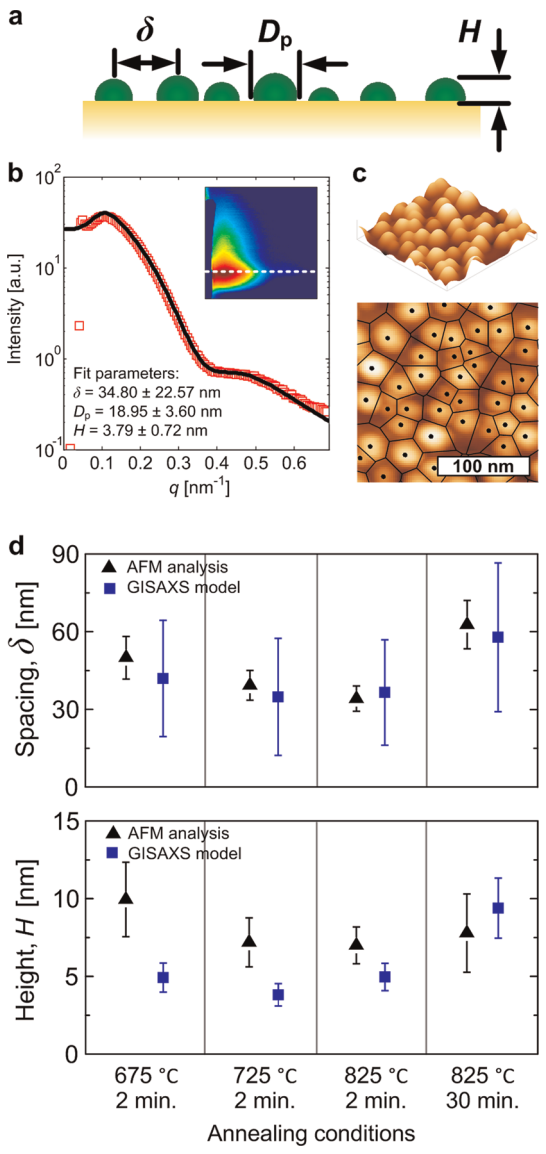

Figure 3. Validation of GISAXS model by quantitative analysis of AFM images. (a) Schematic of 1-D model of catalyst particle array as population of truncated spheres with polydispersity in both size and spacing. (b) *Ex situ* GISAXS data (red square) and model fitting (black line) of Fe particles formed by rapid heating and 2 min annealing in H_2/He at 725 °C. The fit parameters are listed on the plot, and the corresponding 2-D image is the inset. (c) Isometric and top views of an AFM image of the same sample, with particle peaks (black circles) and Voronoi tessellation (black lines) indicated. (d) Comparison of GISAXS fit results with AFM analysis for particle spacing and particle height. Marker and error bar represent population mean and ± standard deviation, respectively.

Figure 3a). The GISAXS intensity collected from the catalyst particles is proportional to the modulus of the form factor squared, $|F(q)|^2$, multiplied by the interference function, $S(q)$,

$$I(q) = |F(q)|^2 S(q) \quad (1)$$

$F(q)$ and $S(q)$ are the Fourier transforms of the catalyst shape and the particle−particle pair correlation function (*i.e.*, spacing), respectively.[42,54,61] The form factor is

$$|F(q)|^2 = A\frac{\int_0^\infty P(R_P)[f_P(q, R_P, H)]^2\, dR_P}{\int_0^\infty P(R_P)\, dR_P} \quad (2)$$

where A is an adjustable constant, R_P is the radius of a sphere (particle) with variance $\sigma_{R_P}{}^2$, and H (height) is the distance from the substrate to the top of a sphere. $P(R_P)$ is the probability density function for the population of particle radii, which accounts for the polydispersity in particle size; f_P is the form factor of the individual scattering body (truncated sphere). There is precedence in the literature to suggest that the particles formed by dewetting of a thin film on a flat substrate have a log-normal size distribution,[62,63] analogous to the size distribution of grains within a solid.[64] As a result, $P(R_P)$ is assigned a log-normal distribution, and we also find that the distribution of particle height, as measured by AFM, is log-normal (99% confidence). Accordingly,

$$P(R_P) = \frac{1}{R_P\sigma_{R_P}\sqrt{2\pi}}\exp\left[\frac{-(\ln R_P - \langle R_P\rangle)^2}{2\sigma {R_P}^2}\right] \quad (3)$$

and

$$f_P(q, R_z, H) = \int_0^H 2\pi {R_z}^2\frac{J_1(qR_z)}{qR_z}dz \quad (4)$$

In the latter equation $R_z = ({R_P}^2 - z^2)^{1/2}$, where z is the vertical coordinate, and J_1 is a Bessel function of the first kind.

The structure factor represents particle−particle scattering, and we use the structure factor for a 1-D paracrystal, which is locally ordered but lacks long-range order. This is

$$S(q) = \frac{1 - e^{-q^2\sigma_\delta{}^2}}{1 + e^{-q^2\sigma_\delta{}^2} - 2e^{-q^2\sigma_\delta{}^2/2}\cos(q\delta)} \quad (5)$$

where δ is the mean particle spacing with variance $\sigma_\delta{}^2$.

According to this model, the spatial distribution of scattered intensity depends on the following independent parameters of the particles: diameter D_P ($2 \times R_P$) and its variance ($\sigma_{D_P}{}^2$), spacing δ and its variance ($\sigma_\delta{}^2$), and height H. Thus, fitting eq 1 to line scans $I(q)$ from the GISAXS data enables us to extract quantitative, statistical information about the population of metal nanoparticles created by dewetting of the Fe film. Fitting is performed by least-squares error minimization using custom code and the MATLAB curve-fitting toolbox.

Validation of GISAXS Model by AFM. In order to validate the GISAXS measurement technique, we compare the fitting results to quantitative analysis of *ex situ* AFM images. For this, we prepared a series of reference samples by annealing Fe/Al_2O_3 films at different

temperatures and durations (Figure S2), and we analyzed each sample using both GISAXS and AFM. After generic AFM image processing using WSxM software,[65] we use custom processing to first identify the positions of all local maxima within each image and then decompose the image by a Voronoi tessellation. A 2-D Voronoi cell is a convex polygon whose segments are the points in the line that are equidistant to the two nearest maxima and whose vertices are the points equidistant to three maxima (Figure 3c). Thus, the Voronoi cell size, defined as the square root of the polygon's area, is a measure of particle−particle nearest neighbor spacing δ (Figure 3d). This type of spatial decomposition is traditionally used to analyze paracrystals and applies to substrate-bound nanoparticles that exhibit only short-range order arising from excluded volume interactions and local coarsening. Further, the particle−particle spacing in the GISAXS model has previously been associated with a distribution of Voronoi cell sizes.[43]

Using AFM images, we determine the height (H) of each particle by subtracting its maximum from the mean roughness of the Al_2O_3, which ranges from 3 to 5 nm depending on annealing conditions (Supporting Information, Figure S2). The shape and diameter of a particle are affected by the tip geometry (which can change with time due to wear) and the tip−sample convolution, so we consider peak height to be a reliable metric from AFM imaging. As a result, the peak height of each particle most accurately captures the distribution of sizes, as opposed to measuring the curvature of the peaks or tallying every pixel. In the latter case, larger particles would be disproportionately weighted because they occupy more pixels than smaller particles.

The summarized results in Figure 3d show that both AFM and GISAXS provide consistent quantitative measures of the mean particle height (H) and spacing δ, for a variety of annealing conditions that result in different film morphologies. We attribute the discrepancy of σ_δ to the decoupling approximation (DA) used in the model,[43] which states that the size of the scattering bodies and their relative positions are not correlated. While DA is typically used only for diffuse systems because it allows for overlapping of the structures, incorporating size-space correlations is challenging for large numbers of images.[40] The GISAXS model also assumes the particles are supported on a flat substrate, whereas the Al_2O_3 support in fact has a finite roughness (Figure S3), which contributes to the disparity in H. Despite these simplifying assumptions, our approach yields good agreement with AFM, thus enabling *in situ* measurement of the catalyst morphology using GISAXS.

SAXS Modeling of CNTs. To relate particle dynamics to CNT growth dynamics, we also adopt a quantitative model of CNT scattering. CNTs are described as a population of hollow cylinders with log-normally distributed outer diameters, as in our previous work.[24,55] The mathematical equations are also reproduced in the Supporting Information for reference. The fitting parameters of the CNT form factor are the outer diameter (D_C) and its variance ($\sigma_{D_C}^2$) and the inner diameter (D_i). The CNT−CNT spacing is ~100 nm ($q \approx 10^{-2}$ nm^{-1}) and therefore above the resolution limit of our setup.[66] This allows us to simplify the expression $I(q)$ for CNTs by setting the structure factor $S(q) = 1$.

Shortly after the hydrocarbon source is added to the reactor, the CNTs comprise a thin, tangled film (Supporting Information, Figure S4), such that GISAXS carries information both from pure Fe particles (without CNTs) and from short CNTs emerging from the Fe particles. By separately fitting the GISAXS scattering during heating and annealing (before CNT nucleation) and the transmission scattering after CNT nucleation, we quantify the dynamics of both catalyst particle formation and CNT growth for a series of thermal and chemical conditions. This enables direct measurement of the CNT size distribution in comparison to the catalyst size distribution. In the next section, we discuss implementation of this analysis methodology to canonical CNT forest growth experiments.

For this work, we collected scattered X-rays at $q \approx 0.1-1.6$ nm^{-1}, which enables measurement of particles and CNTs in the range of ~3−30 nm. The measurement range depends on the area of the detector and the sample-to-detector distance. Smaller nanostructures (*i.e.*, single-wall CNTs) can be measured by collecting X-rays at larger q values, but samples should be sufficiently monodisperse to produce defined scattering peaks, which can be practically fit by mathematical models.

Dynamics of Particle Formation and CNT Nucleation. First, we study the dynamics when the substrate is rapidly heated (100 °C s^{-1}) to 800 °C in H_2/He (Figure 4a). The film rapidly dewets to form particles, starting when the substrate reaches 350 °C (11 s after heating begins). At this instant, D_P and σ_{D_P} both increase rapidly, and they saturate at 17 s. The particle size distribution then remains constant at $D_P = 11.7 \pm 2.1$ nm for the rest of the 2 min annealing step. The diameter of CNTs at the start of growth ($D_C = 12.0 \pm 4.3$ nm) is very close to the measured average particle diameter, although the variance is approximately doubled. However, within 10 s after nucleation, the CNT diameter distribution rapidly shifts downward, and the distribution (σ_{D_C}) focuses, reaching $\sigma_{D_C} = 2.6$ nm. High-resolution SEM imaging of the top of the forest, representing the beginning of growth, gives $D_C = 10.6 \pm 1.8$ nm. This confirms that SAXS accurately measures the CNTs present at the start of the growth process. This value is shown as the black data point superimposed in Figure 4a, and more details are in the Supporting Information (Figure S5).

The subsequent downward shifts in D_C and σ_{D_C} suggest that newly nucleating CNTs overwhelm the

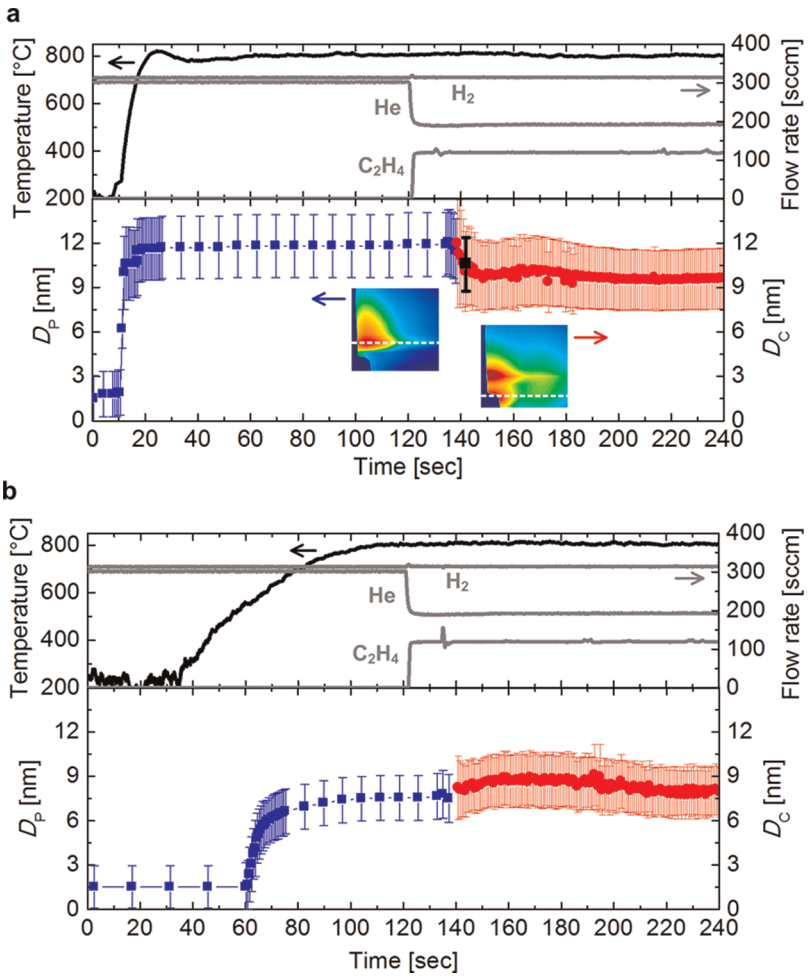

Figure 4. Dynamics of particle formation and CNT nucleation by fitting of real-time GISAXS and SAXS image sequences. Time evolution of particle diameter (blue, left axis) and CNT diameter (red, right axis) for (a) rapid heating and (b) slow heating. Marker and error bar represent population mean and ± standard deviation, respectively. Both experiments are in H_2/He and reach a steady temperature of 800 °C. The corresponding synthesis conditions *versus* time (*i.e.*, temperature and gas flows) are shown above each plot of the diameter dynamics. The inset GISAXS images in (a) show the position on the PAD where the line scan (white dashed line) was taken for data analysis, and the black square near t = 140 s denotes the mean CNT diameter as measured in SEM (see Supporting Information, Figure S5).

existing population with time. The shift in mean CNT diameter is not due to the diameters of individual CNTs changing with time. Indeed, previous studies of isolated, millimeter-long CNTs have shown that diameter and chirality changes typically do not occur during growth,[67] unless a process variable such as temperature[68,69] is modulated. Our explanation of the early shift in mean diameter is also consistent with our recent observations that CNT number density increases up to 10 times during the initial stages of CNT forest growth.[22] This initial density increase is corroborated by increased X-ray scattering intensity measured *in situ*, which is discussed later (Figure 6c). For reference, additional data and fit parameters from this experiment are reported in the Supporting Information (Figure S6).

While rapid heating and annealing is an attractive approach for high-rate continuous manufacturing of CNTs, slower heating is typical in most laboratory processes that are limited by the thermal mass of hot-wall systems (*e.g.*, tube furnaces). Under relatively slow heating (10 °C s^{-1}) in H_2/He, the film dewets at approximately 550 °C (60 s after heating begins), and compared to the rapid heating experiment, the subsequent increase of particle diameter (Figure 4b) is more gradual and is slower to reach a steady value (~100 s). The particle diameter continues to change in the presence of increasing C_2H_4 partial pressure until CNTs nucleate (past which accurate quantification of particles is difficult). While the mean CNT diameter for this case is also dynamic during early growth, σ_{D_C} remains comparatively more stable and smaller overall. Thus, the heating rate influences the size and monodispersity of the nanoparticles, and in these experiments a slower heating rate in H_2/He results in smaller diameter CNTs with lower variance.

While we find that the film dewets very rapidly in H_2/He, previous studies have suggested that continued

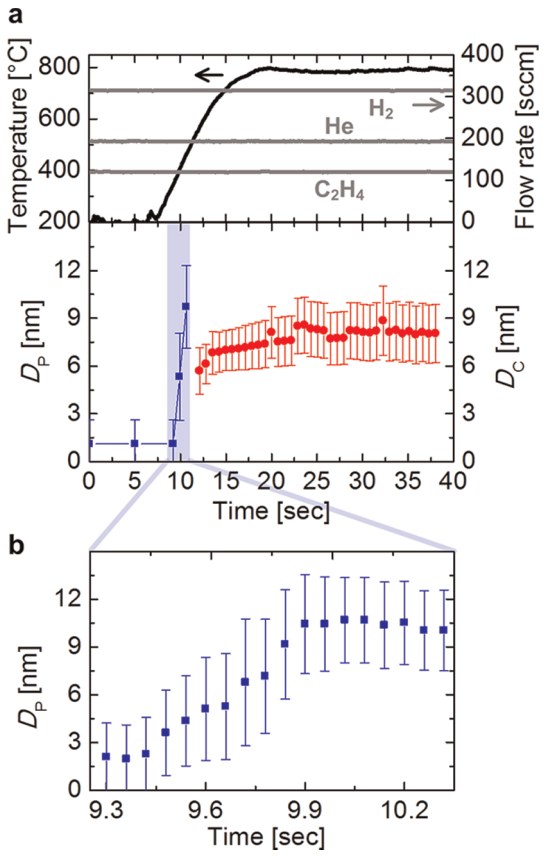

Figure 5. (a) Time evolution of particle diameter (blue, left axis) and CNT diameter (red, right axis) during rapid heating in C_2H_4/H_2/He (set point value 800 °C). Marker indicates the mean value, and the error bar is ± the standard deviation. The corresponding temperature and gas flows are shown above each plot of the diameter dynamics. (b) Expanded time scale corresponding to the shaded blue region in (a), which shows quantification of the film dynamics 60 ms time steps (limit is 10 ms). Under these conditions, the film dewets in approximately 0.5 s.

annealing in H_2/He causes coarsening of the particles.[34,70] As a result, an increasingly common practice for CNT synthesis is to rapidly heat the catalyst film in the presence of both hydrocarbon and H_2 precursors, aiming also to achieve smaller diameter CNTs and further reduce the process time.[71,72] Figure 5a shows results where the substrate was heated rapidly (100 °C s^{-1}) in C_2H_4/H_2/He. In this case, the film begins to dewet at approximately 350 °C, and the particle diameter (D_P = 10.4 ± 2.7 nm) is close to the value obtained by rapid heating in H_2/He. However, the first CNTs observed in transmission scattering are much smaller (D_C = 5.7 ± 1.5 nm) than after pretreating in H_2/He and, interestingly, are smaller than the particles that are detected immediately upon dewetting. This suggests that heating the catalyst film in the presence of active carbon precursors creates and/or activates a subpopulation of catalysts of smaller average diameter. However, as time proceeds, the CNT population evolves to D_C = 9.2 ± 2.1 nm, which is closer to the initial size of the catalysts. Thus, the smaller subpopulation either is not stable to support prolonged CNT growth or is overwhelmed by the main population of larger particles and corresponding larger CNTs. This experiment also demonstrates the time resolution of our technique. For instance, Figure 5b shows that we quantify changes in the catalyst film morphology with time steps of 60 ms, but in principle the limit is *10 ms*, given the frame rate of the pixel array detector. Here, we clearly resolve the particle scattering signature before CNT scattering appears, thus confirming that dewetting of the film into approximately hemispherical islands is a distinct step of the process, even in the presence of hydrocarbons.

During the initial heating, the Fe film, which is oxidized when exposed to ambient, reduces to its metallic state,[36] dewets, and forms stable islands (particles). When the substrate is heated in an inert atmosphere (*i.e.*, He) we do not observe dewetting. Thus, a reducing atmosphere, which evidently affects the mobility of the Fe atoms, is important for transforming a thin film into particles. Overall, the dewetting of the Fe film is driven by instability induced by surface tension and thermal stress, which arises from mismatch in coefficients of thermal expansion between the film and its support.[73−77] There is a net decrease in free energy when the film restructures into hemispherical particles by surface diffusion of Fe. After dewetting, the subsequent rate of particle coarsening is expected to decay exponentially[74,76] as the system tends toward equilibrium. The equilibrium size and shape (contact angle) of the catalyst particles are related to the free energy balance of the lower energy surface of the Al_2O_3 support with that of the Fe,[78] and herein we show that the heating rate also influences the resultant particle geometry.

In all of our experiments, we find that rapid dewetting is followed by relatively slow coarsening of the particles. Although we observe that the Fe particles remain relatively stable over the 2 min annealing step in H_2/He, our AFM data in Figure 3d and additional *in situ* GISAXS studies (Supporting Information, Figure S7) clearly show that particle size and spacing increase gradually over a longer duration. This complements recent studies that show populations of Fe nanoparticles on Al_2O_3 can coarsen significantly during annealing.[34,35] However, the particles in these recent studies are smaller than those found in our work, and we expect smaller particles to coarsen more quickly. Combining all these insights, it is apparent that the dynamic behavior of CNT catalyst populations is related to their size, the surface properties of the substrate, and the processing conditions.

Dynamics of CNT Self-Organization. Finally, we demonstrate that GISAXS enables quantification of the dynamics of CNT self-organization into a vertically aligned forest. The CNT alignment is quantified by integrating the scattered intensity along the azimuthal

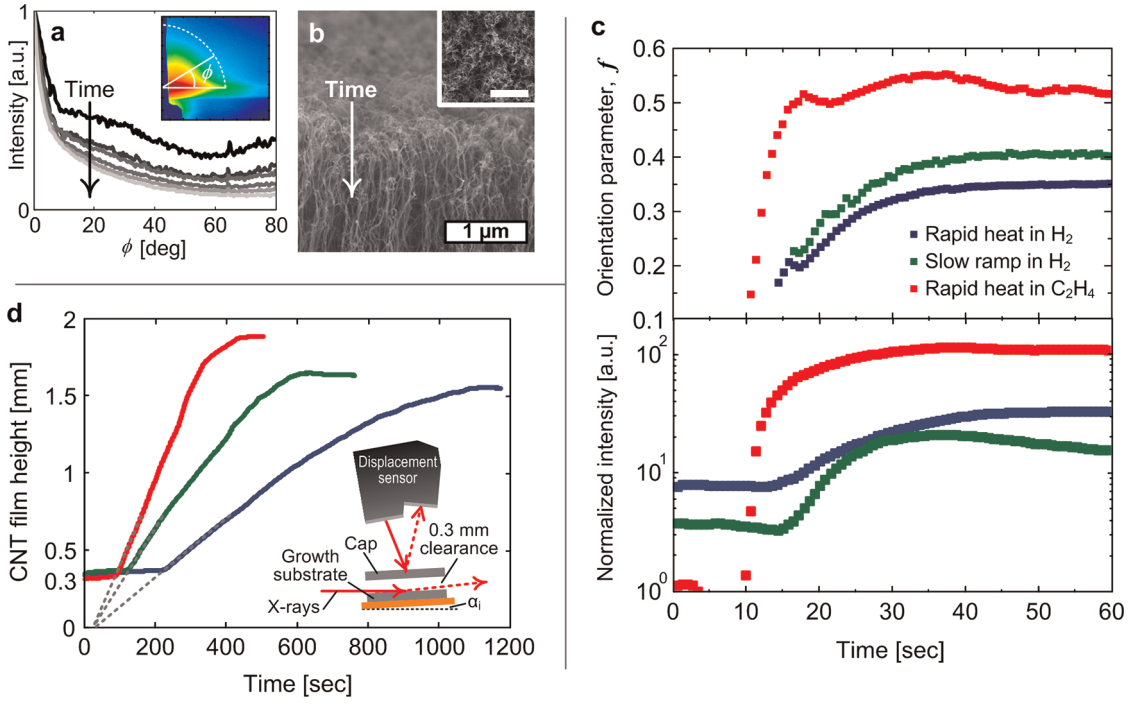

Figure 6. ***In situ*** **observation of self-organization of CNTs into a vertically aligned forest. (a) Representative data showing the evolution in CNT alignment** ***via*** **normalized scattering intensity plotted** ***versus*** ϕ**, the azimuthal angle about the axis of the X-ray beam. (b) Side view SEM image of the tangled "crust" morphology at the top of a CNT forest. (c) Time-resolved X-ray scattering characterization of CNTs for the three different annealing conditions, showing both orientation parameter and integrated scattering intensity, which is normalized to the initial intensity (measured before heating and C_2H_4 injection). (d) Corresponding CNT film height kinetics for the annealing cases shown in Figure 4 and 5. Inset shows experimental setup has a clearance of 0.3 mm, which allows the X-ray beam to probe the Fe surface as well as capture height kinetics once the CNT film begins to grow (not drawn to scale). Thus, height measurements begin at 0.3 mm, and we draw a linear extrapolation (gray dashed) to estimate the kinetics for** $h < 0.3$ **mm. All experiments are at 800 °C.**

angle ϕ (about the beam's axis), as shown in Figure 6a. The intensity distribution is an indication of the average CNT orientation within the beam path. As in our previous work,[21,24,79] we quantify orientation using the parameter[80]

$$f = \frac{1}{2}(3\langle\cos^2\phi\rangle - 1) \quad (6)$$

where

$$\langle\cos^2\phi\rangle = \frac{\int_0^{\pi/2}[I(\phi)\sin\phi\cos^2\phi]\mathrm{d}\phi}{\int_0^{\pi/2}[I(\phi)\sin\phi]\mathrm{d}\phi} \quad (7)$$

Values of f equal to -0.5, 0, and 1, correspond to perfectly horizontal, random (disordered), and perfectly vertical orientations, respectively. Therefore, by calculating f for each sequential scattering image we quantify the evolution of alignment as CNT growth proceeds with time. Note that the azimuthal scan is performed at $q \approx 0.8\ \mathrm{nm}^{-1}$, which is the location of the CNT signature peak. This is important so as not to confuse the catalyst scattering with that of the CNTs, since for a period there are contributions from both nanostructures in the GISAXS images (Figure 2c). Also, there is inherent anisotropy in GISAXS patterns because of the multiple scattering effects along the horizon that arise from the substrate.[40] Nevertheless, we can still definitively identify and quantitatively monitor alignment using this approach.

We show that CNT alignment increases and then saturates; we associate this increase during early growth with a transition from the ubiquitous tangled "crust" at the top of CNT forests (*i.e.*, beginning of growth)[21,27,28] to the vertically aligned morphology (Figure 6b). Note that in order to directly compare data from different experiments, time equals zero in Figure 6c,d corresponds to the point at which CNT growth is initiated, either by introducing C_2H_4 to the heated catalyst or by heating the catalyst in an environment of C_2H_4. We expect that this increase of alignment is due to an increasing number density of CNTs,[22] which is corroborated by an increase in total scattering intensity (Figure 6c). The increase of alignment is influenced by increased van der Waals forces between CNTs as the existing CNTs grow longer; thus, in combination with increasing number density of CNTs, self-alignment is a cooperative effect. The transient increase in alignment is sublinear with growth time, and the saturation of f is concomitant with the beginning of upward forest growth. Thus, we show there is a critical threshold of alignment necessary for CNTs to self-organize into a

forest (*i.e.*, to "lift off" from the substrate; Figure S8). We expect that, depending on the diameter and straightness of the CNTs, there is a density at which the transition occurs. This critical density for self-organization is analogous to the density decay that suddenly interrupts the self-aligned morphology and leads to abrupt termination of CNT forest growth. We previously measured this critical density to be $\sim 1 \times 10^9$ CNTs cm^{-2}.[21,22]

When the substrate is heated rapidly in the presence of thermally treated C_2H_4 (with H_2/He), we observe accelerated self-organization (3×) and a higher final value of the orientation parameter compared to annealing in H_2/He alone. It is also interesting that the rate at which the transition occurs correlates with the average growth rate r_{av} of the forest with $r_{av} = 1.7$, 3.1, and 5.6 $\mu m\ s^{-1}$ for forests shown in Figure 4a,b and Figure 5, respectively. Namely, steeper height kinetics corresponds to a faster transition to the vertically aligned morphology. This suggests that the transition is at least in part governed by the lengthening rate of constituent CNTs, in conjunction with increasing density. While we believe this is the first study to quantify this transition *in situ* during CNT synthesis, we are reminded of the isotropic−nematic (aligned) phase changes previously observed both experimentally in CNT solutions[81−83] and DNA[84] and in numerical models of rod-shaped molecules (for study of liquid crystals).[85−87] The latter body of work has built upon phase diagrams predicting that increased aspect ratio (*i.e.*, length) and/or packing density of the rods can induce the transition from disordered to higher order phases based on excluded volume interactions (*i.e.*, van der Waals).[88] Combining these insights with additional analysis and modeling may allow us to relate the dynamics and mechanics of self-organization to the CNT diameter and attractive forces. The forces that evolve between adjacent CNTs during this stage are implicitly essential to the morphology of the film and also may influence the maximum density of CNTs.

CONCLUSIONS

We show that *in situ* X-ray scattering enables nondestructive interrogation of the dynamics of collective CNT growth, including catalyst film dewetting and particle coarsening, CNT nucleation, and CNT self-organization into vertically aligned forests. Mathematical models of time-resolved scattering patterns are used to quantify the evolution of catalyst and CNT populations. The size and monodispersity of the catalyst particles are influenced by the heating rate, and while the CNT diameters that nucleate are similar to those of the catalysts initially, the CNT population typically evolves rapidly during nucleation. Further, vertically aligned growth begins abruptly once the average CNT orientation reaches a critical threshold, which depends on the process conditions. Our use of synchrotron radiation and a high-speed detector is a powerful high-speed diagnostic tool for nanomaterials production and will be useful to devise feedback control schemes to optimize synthesis conditions *in situ*. The technique may also be useful to engineer nanoparticle arrays for *in situ* catalytic studies and to explore the growth and self-assembly of other one-dimensional nanostructures.

Conflict of Interest: The authors declare no competing financial interest.

Acknowledgment. Financial support was provided by the Office of Naval Research (N00014101055) for scattering model development, data analysis, and manuscript preparation; the National Science Foundation (NSF) Nanomanufacturing Program (CMMI-0800213) for data collection; and startup funds from the University of Michigan Department of Mechanical Engineering and College of Engineering for equipment setup. X-ray scattering was performed in the G1 beamline at the Cornell High-Energy Synchrotron Source (CHESS), which is supported by the NSF and NIH-NIGMS under NSF Grant DMR-0936384. Detector development at Cornell is supported by DOE awards FG02-97ER62443 and DE-FG02-10ER46693, a subcontract under DOE contract DEAC02-76SF00515, and the Keck Foundation. E.V. thanks the Eastman Kodak Corporation and the Kodak Fellows Program for support. We thank Ryan Bennett, Michaël De Volder, Sangwoo Han, Anne Juggernauth, Jeremy Ng, Jong Ok, Myounggu Park, Ben Wang, Kyle Yazzie, and Yongyi Zhang for assistance with X-ray scattering measurements, data processing, and equipment setup. We also thank Namiko Yamamoto at MIT for preparation of catalyst substrates. Microscopy was performed at the University of Michigan Electron Microbeam Analysis Library (EMAL).

Supporting Information Available: Mathematical model for SAXS of CNTs, mass spectrometry data, AFM images of annealed catalyst films, SEM of CNTs, additional data and fitting parameters for *in situ* experiments, as well as videos of real-time X-ray images during catalyst annealing, CNT nucleation, and CNT self-organization. This material is available free of charge *via* the Internet at http://pubs.acs.org.

REFERENCES AND NOTES

1. Nihei, M.; Horibe, M.; Kawabata, A.; Awano, Y. Simultaneous Formation of Multiwall Carbon Nanotubes and Their End-Bonded Ohmic Contacts to Ti Electrodes for Future VLSI Interconnects. *Jpn. J. Appl. Phys.* **2004**, *43*, 1856–1859.
2. Horibe, M.; Nihei, M.; Kondo, D.; Kawabata, A.; Awano, Y. Carbon Nanotube Growth Technologies Using Tantalum Barrier Layer for Future Ulsis with Cu/Low-K Interconnect Processes. *Jpn. J. Appl. Phys.* **2005**, *44*, 5309–5312.
3. Nihei, M.; Kawabata, A.; Kondo, D.; Horibe, M.; Sato, S.; Awano, Y. Electrical Properties of Carbon Nanotube Bundles for Future *via* Interconnects. *Jpn. J. Appl. Phys.* **2005**, *44*, 1626–1628.
4. Kreupl, F.; Graham, A. P.; Duesberg, G. S.; Steinhogl, W.; Liebau, M.; Unger, E.; Honlein, W. Carbon Nanotubes in Interconnect Applications. *Microelectron. Eng.* **2002**, *64*, 399–408.
5. Chiodarelli, N.; Li, Y.; Cott, D. J.; Mertens, S.; Peys, N.; Heyns, M.; De Gendt, S.; Groeseneken, G.; Vereecken, P. M. Integration and Electrical Characterization of Carbon Nanotube *via* Interconnects. *Microelectron. Eng.* **2011**, *88*, 837–843.
6. Wu, Z.; Chen, Z.; Du, X.; Logan, J. M.; Sippel, J.; Nikolou, M.; Kamaras, K.; Reynolds, J. R.; Tanner, D. B.; Hebard, A. F.; Rinzler, A. G. Transparent, Conductive Carbon Nanotube Films. *Science* **2004**, *305*, 1273–1276.
7. Zhu, L. B.; Sun, Y. Y.; Hess, D. W.; Wong, C. P. Well-Aligned Open-Ended Carbon Nanotube Architectures: An Approach for Device Assembly. *Nano Lett.* **2006**, *6*, 243–247.

8. Sohn, J.; Lee, S.; Song, Y.; Choi, S.; Cho, K.; Nam, K. Patterned Selective Growth of Carbon Nanotubes and Large Field Emission from Vertically Well-Aligned Carbon Nanotube Field Emitter Arrays. *Appl. Phys. Lett.* **2001**, *78*, 901–903.
9. Pan, Z. W.; Au, F. C. K.; Lai, H. L.; Zhou, W. Y.; Sun, L. F.; Liu, Z. Q.; Tang, D. S.; Lee, C. S.; Lee, S. T.; Xie, S. S. Very Low-Field Emission from Aligned and Opened Carbon Nanotube Arrays. *J. Phys. Chem. B* **2001**, *105*, 1519–1522.
10. Huang, H.; Liu, C. H.; Wu, Y.; Fan, S. S. Aligned Carbon Nanotube Composite Films for Thermal Management. *Adv. Mater.* **2005**, *17*, 1652–1656.
11. Tong, T.; Zhao, Y.; Delzeit, L.; Kashani, A.; Meyyappan, M.; Majumdar, A. Dense, Vertically Aligned Multiwalled Carbon Nanotube Arrays as Thermal Interface Materials. *IEEE Trans. Compon., Packag. Technol.* **2007**, *30*, 92–100.
12. Holt, J.; Park, H.; Wang, Y.; Stadermann, M.; Artyukhin, A.; Grigoropoulos, C.; Noy, A.; Bakajin, O. Fast Mass Transport through Sub-2-Nanometer Carbon Nanotubes. *Science* **2006**, *312*, 1034–1037.
13. Hinds, B.; Chopra, N.; Rantell, T.; Andrews, R.; Gavalas, V.; Bachas, L. Aligned Multiwalled Carbon Nanotube Membranes. *Science* **2004**, *303*, 62–65.
14. Garcia, E. J.; Wardle, B. L.; Hart, A. J. Joining Prepreg Composite Interfaces With Aligned Carbon Nanotubes. *Compos. Part A* **2008**, *39*, 1065–1070.
15. De Volder, M.; Tawfick, S. H.; Park, S. J.; Copic, D.; Zhao, Z.; Lu, W.; Hart, A. J. Diverse 3D Microarchitectures Made by Capillary Forming of Carbon Nanotubes. *Adv. Mater.* **2010**, *22*, 4384–4389.
16. Kempa, K.; Kimball, B.; Rybczynski, J.; Huang, Z. P.; Wu, P. F.; Steeves, D.; Sennett, M.; Giersig, M.; Rao, D. V. G. L. N.; Carnahan, D. L.; *et al*. Photonic Crystals Based on Periodic Arrays of Aligned Carbon Nanotubes. *Nano Lett.* **2002**, *3*, 13–18.
17. Lidorikis, E.; Ferrari, A. C. Photonics With Multiwall Carbon Nanotube Arrays. *ACS Nano* **2009**, *3*, 1238–1248.
18. Prasher, R. S.; Hu, X. J.; Chalopin, Y.; Mingo, N.; Lofgreen, K.; Volz, S.; Cleri, F.; Keblinski, P. Turning Carbon Nanotubes from Exceptional Heat Conductors into Insulators. *Phys. Rev. Lett.* **2009**, 102.
19. Duong, H. M.; Yamamoto, N.; Papavassiliou, D. V.; Maruyama, S.; Wardle, B. L. Inter-Carbon Nanotube Contact in Thermal Transport of Controlled-Morphology Polymer Nanocomposites. *Nanotechnology* **2009**, 20.
20. Nirmalraj, P. N.; Lyons, P. E.; De, S.; Coleman, J. N.; Boland, J. J. Electrical Connectivity in Single-Walled Carbon Nanotube Networks. *Nano Lett.* **2009**, *9*, 3890–3895.
21. Bedewy, M.; Meshot, E.; Guo, H.; Verploegen, E.; Lu, W.; Hart, A. Collective Mechanism for the Evolution and Self-Termination of Vertically Aligned Carbon Nanotube Growth. *J. Phys. Chem. C* **2009**, *113*, 20576–20582.
22. Bedewy, M.; Meshot, E. R.; Reinker, M. J.; Hart, A. J. Population Growth Dynamics Of Carbon Nanotubes. *ACS Nano* **2011**, *5*, 8974–8989.
23. Han, J. H.; Graff, R. A.; Welch, B.; Marsh, C. P.; Franks, R.; Strano, M. S. A Mechanochemical Model of Growth Termination in Vertical Carbon Nanotube Forests. *ACS Nano* **2008**, *2*, 53–60.
24. Wang, B.; Bennett, R.; Verploegen, E.; Hart, A.; Cohen, R. Quantitative Characterization of the Morphology of Multiwall Carbon Nanotube Films by Small-Angle X-Ray Scattering. *J. Phys. Chem. C* **2007**, *111*, 5859–5865.
25. Wang, H.; Xu, Z.; Eres, G. Order in Vertically Aligned Carbon Nanotube Arrays. *Appl. Phys. Lett.* **2006**, *88*, 213111.
26. Vinten, P.; Bond, J.; Marshall, P.; Lefebvre, J.; Finnie, P. Origin of Periodic Rippling during Chemical Vapor Deposition Growth of Carbon Nanotube Forests. *Carbon* **2011**, *49*, 4972–4981.
27. Zhang, L.; Li, Z.; Tan, Y.; Lolli, G.; Sakulchaicharoen, N.; Requejo, F.; Mun, B.; Resasco, D. Influence of a Top Crust of Entangled Nanotubes on the Structure of Vertically Aligned Forests of Single-Walled Carbon Nanotubes. *Chem. Mater.* **2006**, *18*, 5624–5629.
28. Zhang, Q.; Zhou, W.; Qian, W.; Xiang, R.; Huang, J.; Wang, D.; Wei, F. Synchronous Growth of Vertically Aligned Carbon Nanotubes with Pristine Stress in the Heterogeneous Catalysis Process. *J. Phys. Chem. C* **2007**, *111*, 14638–14643.
29. Einarsson, E.; Murakami, Y.; Kadowaki, M.; Maruyama, S. Growth Dynamics of Vertically Aligned Single-Walled Carbon Nanotubes from *in Situ* Measurements. *Carbon* **2008**, *46*, 923–930.
30. Xiang, R.; Yang, Z.; Zhang, Q.; Luo, G.; Qian, W.; Wei, F.; Kadowaki, M.; Einarsson, E.; Maruyama, S. Growth Deceleration of Vertically Aligned Carbon Nanotube Arrays: Catalyst Deactivation or Feedstock Diffusion Controlled? *J. Phys. Chem. C* **2008**, *112*, 4892–4896.
31. Hasegawa, K.; Noda, S. Millimeter-Tall Single-Walled Carbon Nanotubes Rapidly Grown with and without Water. *ACS Nano* **2011**, *5*, 975–984.
32. Puretzky, A. A.; Geohegan, D. B.; Schittenhelm, H.; Fan, X.; Guillorn, M. A. Time-Resolved Diagnostics of Single Wall Carbon Nanotube Synthesis by Laser Vaporization. *Appl. Surf. Sci.* **2002**, *197—198*, 552–562.
33. Harutyunyan, A. R.; Chen, G.; Paronyan, T. M.; Pigos, E. M.; Kuznetsov, O. A.; Hewaparakrama, K.; Kim, S. M.; Zakharov, D.; Stach, E. A.; Sumanasekera, G. U. Preferential Growth of Single-Walled Carbon Nanotubes with Metallic Conductivity. *Science* **2009**, *326*, 116–120.
34. Kim, S. M.; Pint, C. L.; Amama, P. B.; Zakharov, D. N.; Hauge, R. H.; Maruyama, B.; Stach, E. A. Evolution in Catalyst Morphology Leads to Carbon Nanotube Growth Termination. *J. Phys. Chem. Lett.* **2010**, *1*, 918–922.
35. Amama, P.; Pint, C.; McJilton, L.; Kim, S.; Stach, E.; Murray, P.; Hauge, R.; Maruyama, B. Role of Water in Super Growth of Single-Walled Carbon Nanotube Carpets. *Nano Lett.* **2009**, *9*, 44–49.
36. Hofmann, S.; Blume, R.; Wirth, C. T.; Cantoro, M.; Sharma, R.; Ducati, C.; Havecker, M.; Zafeiratos, S.; Schnoerch, P.; Oestereich, A.; *et al*. State of Transition Metal Catalysts during Carbon Nanotube Growth. *J. Phys. Chem. C* **2009**, *113*, 1648–1656.
37. Mattevi, C.; Wirth, C. T.; Hofmann, S.; Blume, R.; Cantoro, M.; Ducati, C.; Cepek, C.; Knop-Gericke, A.; Milne, S.; Castellarin-Cudia, C.; *et al*. *In-Situ* X-Ray Photoelectron Spectroscopy Study of Catalyst-Support Interactions and Growth of Carbon Nanotube Forests. *J. Phys. Chem. C* **2008**, *112*, 12207–12213.
38. Hofmann, S.; Sharma, R.; Ducati, C.; Du, G.; Mattevi, C.; Cepek, C.; Cantoro, M.; Pisana, S.; Parvez, A.; Cervantes-Sodi, F.; *et al*. *In Situ* Observations of Catalyst Dynamics during Surface-Bound Carbon Nanotube Nucleation. *Nano Lett.* **2007**, *7*, 602–608.
39. Picher, M.; Anglaret, E.; Arenal, R.; Jourdain, V. Self-Deactivation of Single-Walled Carbon Nanotube Growth Studied by *in Situ* Raman Measurements. *Nano Lett.* **2009**, *9*, 542–547.
40. Renaud, G.; Lazzari, R.; Leroy, F. Probing Surface and Interface Morphology with Grazing Incidence Small Angle X-Ray Scattering. *Surf. Sci. Rep.* **2009**, *64*, 255–380.
41. Revenant, C.; Leroy, F.; Lazzari, R.; Renaud, G.; Henry, C. R. Quantitative Analysis of Grazing Incidence Small-Angle X-Ray Scattering: Pd/MgO(001) Growth. *Phys. Rev. B* **2004**, *69*, 035411.
42. Renaud, G.; Lazzari, R.; Revenant, C.; Barbier, A.; Noblet, M.; Ulrich, O.; Leroy, F.; Jupille, J.; Borensztein, Y.; Henry, C. R.; *et al*. Real-Time Monitoring of Growing Nanoparticles. *Science* **2003**, *300*, 1416–1419.
43. Lazzari, R.; Renaud, G.; Jupille, J.; Leroy, F. Self-Similarity During Growth of the Au/TiO_2 (110) Model Catalyst as Seen by the Scattering of X-Rays at Grazing-Angle Incidence. *Phys. Rev. B* **2007**, *76*, 125412.
44. Abecassis, B.; Testard, F.; Spalla, O.; Barboux, P. Probing *in Situ* the Nucleation and Growth of Gold Nanoparticles by Small-Angle X-Ray Scattering. *Nano Lett.* **2007**, *7*, 1723–1727.
45. Abecassis, B.; Testard, F.; Spalla, O. Gold Nanoparticle Superlattice Crystallization Probed *in Situ*. *Phys. Rev. Lett.* **2008**, *100*, 115504.
46. Beaucage, G.; Kammler, H. K.; Pratsinis, S. E. Particle Size Distributions from Small-Angle Scattering Using Global

Scattering Functions. *J. Appl. Crystallogr.* **2004**, *37*, 523–535.
47. Beaucage, G.; Kammler, H. K.; Mueller, R.; Strobel, R.; Agashe, N.; Pratsinis, S. E.; Narayanan, T. Probing the Dynamics of Nanoparticle Growth in a Flame Using Synchrotron Radiation. *Nat. Mater.* **2004**, *3*, 370–373.
48. Sztucki, M.; Narayanana, T.; Beaucage, G. *In Situ* Study of Aggregation of Soot Particles in an Acetylene Flame by Small-Angle X-Ray Scattering. *J. Appl. Phys.* **2007**, *101*, 114304.
49. van Laake, L.; Hart, A. J.; Slocum, A. H. Suspended Heated Silicon Platform for Rapid Thermal Control of Surface Reactions with Application to Carbon Nanotube Synthesis. *Rev. Sci. Instrum.* **2007**, 78.
50. Meshot, E.; Hart, A. Abrupt Self-Termination of Vertically Aligned Carbon Nanotube Growth. *Appl. Phys. Lett.* **2008**, *92*, 113107.
51. Henderson, S. Comparison of Parasitic Scattering from Window Materials Used for Small-Angle X-Ray Scattering: A Better Beryllium Window. *J. Appl. Crystallogr.* **1995**, *28*, 820–826.
52. Koerner, L. J.; Philipp, H. T.; Hromalik, M. S.; Tate, M. W.; Gruner, S. M. X-Ray Tests of a Pixel Array Detector for Coherent X-Ray Imaging at the Linac Coherent Light Source. *J. Instrum.* **2009**, *4*, P03001.
53. Philipp, H.; Koerner, L.; Hromalik, M.; Tate, M.; Gruner, S. Femtosecond Radiation Experiment Detector for X-Ray Free-Electron Laser (XFEL) Coherent X-Ray Imaging. *IEEE T. Nucl. Sci.* **2010**, *57*, 3795–3799.
54. Levine, J. R.; Cohen, J. B.; Chung, Y. W.; Georgopoulos, P. Grazing-Incidence Small-Angle X-Ray Scattering: New Tool for Studying Thin Film Growth. *J. Appl. Crystallogr.* **1989**, *22*, 528–532.
55. Meshot, E.; Plata, D.; Tawfick, S.; Zhang, Y.; Verploegen, E.; Hart, A. Engineering Vertically Aligned Carbon Nanotube Growth by Decoupled Thermal Treatment of Precursor and Catalyst. *ACS Nano* **2009**, *3*, 2477–2486.
56. Plata, D. L.; Hart, A. J.; Reddy, C. M.; Gschwend, P. M. Early Evaluation of Potential Environmental Impacts of Carbon Nanotube Synthesis by Chemical Vapor Deposition. *Environ. Sci. Technol.* **2009**, *43*, 8367–8373.
57. Hart, A. J.; Slocum, A. Rapid Growth and Flow-Mediated Nucleation of Millimeter-Scale Aligned Carbon Nanotube Structures from a Thin-Film Catalyst. *J. Phys. Chem. B* **2006**, *110*, 8250–8257.
58. Kukovitsky, E. F.; L'Vov, S. G.; Sainov, N. A.; Shustov, V. A.; Chernozatonskii, L. A. Correlation between Metal Catalyst Particle Size and Carbon Nanotube Growth. *Chem. Phys. Lett.* **2002**, *355*, 497–503.
59. Nerushev, O. A.; Dittmar, S.; Morjan, R. E.; Rohmund, F.; Campbell, E. E. B. Particle Size Dependence and Model for Iron-Catalyzed Growth of Carbon Nanotubes by Thermal Chemical Vapor Deposition. *J. Appl. Phys.* **2003**, *93*, 4185–4190.
60. Plata, D.; Meshot, E.; Reddy, C.; Hart, A.; Gschwend, P. Multiple Alkynes React with Ethylene to Enhance Carbon Nanotube Synthesis, Suggesting a Polymerization-Like Formation Mechanism. *ACS Nano* **2010**, *4*, 7185–7192.
61. Rauscher, M.; Paniago, R.; Metzger, H.; Kovats, Z.; Domke, J.; Peisl, J.; Pfannes, H.; Schulze, J.; Eisele, I. Grazing Incidence Small Angle X-Ray Scattering from Free-Standing Nanostructures. *J. Appl. Phys.* **1999**, *86*, 6763–6769.
62. Söderlund, J.; Kiss, L. B.; Niklasson, G. A.; Granqvist, C. G. Lognormal Size Distributions in Particle Growth Processes without Coagulation. *Phys. Rev. Lett.* **1998**, *80*, 2386–2388.
63. Kiss, L. B.; Söderlund, J.; Niklasson, G. A.; Granqvist, C. G. New Approach to the Origin of Lognormal Size Distributions of Nanoparticles. *Nanotechnology* **1999**, *10*, 25.
64. Thompson, C. V. Coarsening of Particles on a Planar Substrate - Interface Energy Anisotropy and Application to Grain-Growth in Thin Films. *Acta Metall.* **1988**, *36*, 2929–2934.
65. Horcas, I.; Fernandez, R.; Gomez-Rodriguez, J.; Colchero, J.; Gomez-Herrero, J.; Baro, A. WSXM: A Software for Scanning Probe Microscopy and a Tool for Nanotechnology. *Rev. Sci. Instrum.* **2007**, *78*, 013705.
66. Verploegen, E. A.; Hart, A. J.; De Volder, M.; Tawfick, S.; Chia, K. K.; Cohen, R. E. Non-Destructive Characterization of Structural Hierarchy within Aligned Carbon Nanotube Assemblies. *J. Appl. Phys.* **2011**, *109*, 094316.
67. Yao, Y.; Li, Q.; Zhang, J.; Liu, R.; Jiao, L.; Zhu, Y. T.; Liu, Z. Temperature-Mediated Growth of Single-Walled Carbon-Nanotube Intramolecular Junctions. *Nat. Mater.* **2007**, *6*, 283–286.
68. Doorn, S. K.; Zheng, L.; O'Connell, M. J.; Zhu, Y.; Huang, S.; Liu, J. Raman Spectroscopy and Imaging of Ultralong Carbon Nanotubes. *J. Phys. Chem. B* **2005**, *109*, 3751–3758.
69. Anderson, N.; Hartschuh, A.; Novotny, L. Chirality Changes in Carbon Nanotubes Studied with Near-Field Raman Spectroscopy. *Nano Lett.* **2007**, *7*, 577–582.
70. Sugime, H.; Noda, S.; Maruyama, S.; Yamaguchi, Y. Multiple "Optimum" Conditions for Co–Mo Catalyzed Growth of Vertically Aligned Single-Walled Carbon Nanotube Forests. *Carbon* **2009**, *47*, 234–241.
71. Pint, C. L.; Pheasant, S. T.; Parra-Vasquez, A. N. G.; Horton, C.; Xu, Y.; Hauge, R. H. Investigation of Optimal Parameters for Oxide-Assisted Growth of Vertically Aligned Single-Walled Carbon Nanotubes. *J. Phys. Chem. C* **2009**, *113*, 4125–4133.
72. Zhang, Y. Y.; Gregoire, J. M.; van Dover, R. B.; Hart, A. J. Ethanol-Promoted High-Yield Growth of Few-Walled Carbon Nanotubes. *J. Phys. Chem. C* **2010**, *114*, 6389–6395.
73. Seemann, R.; Herminghaus, S.; Jacobs, K. Dewetting Patterns and Molecular Forces: A Reconciliation. *Phys. Rev. Lett.* **2001**, *86*, 5534.
74. Jiran, E.; Thompson, C. V. Capillary Instabilities in Thin, Continuous Films. *Thin Solid Films* **1992**, *208*, 23–28.
75. Thompson, C. V.; Carel, R. Stress and Grain Growth in Thin Films. *J. Mech. Phys. Solids* **1996**, *44*, 657–673.
76. Srolovitz, D.; Safran, S. Capillary Instabilities in Thin-Films. II. Kinetics. *J. Appl. Phys.* **1986**, *60*, 255–260.
77. Srolovitz, D. J. On the Stability of Surfaces of Stressed Solids. *Acta Metall.* **1989**, *37*, 621–625.
78. Danielson, D. T. Surface-Energy-Driven Dewetting Theory of Silicon-On-Insulator Agglomeration. *J. Appl. Phys.* **2006**, *100*, 083507.
79. Meshot, E.; Bedewy, M.; Lyons, K.; Woll, A.; Juggernauth, K.; Tawfick, S.; Hart, A. Measuring the Lengthening Kinetics of Aligned Nanostructures by Spatiotemporal Correlation of Height and Orientation. *Nanoscale* **2010**, 896–900.
80. Hermans, P. H. *Contribution to the Physics of Cellulose Fibres: A Study in Sorption, Density, Refractive Power and Orientation*; Elsevier Pub. Co.: Amsterdam, 1946.
81. Song, W. H.; Kinloch, I. A.; Windle, A. H. Nematic Liquid Crystallinity of Multiwall Carbon Nanotubes. *Science* **2003**, *302*, 1363–1363.
82. Rai, P. K.; Pinnick, R. A.; Parra-Vasquez, A. N. G.; Davis, V. A.; Schmidt, H. K.; Hauge, R. H.; Smalley, R. E.; Pasquali, M. Isotropic–Nematic Phase Transition of Single-Walled Carbon Nanotubes in Strong Acids. *J. Am. Chem. Soc.* **2005**, *128*, 591–595.
83. Shaffer, M. S. P.; Fan, X.; Windle, A. H. Dispersion and Packing of Carbon Nanotubes. *Carbon* **1998**, *36*, 1603–1612.
84. Nakata, M.; Zanchetta, G.; Chapman, B. D.; Jones, C. D.; Cross, J. O.; Pindak, R.; Bellini, T.; Clark, N. A. End-To-End Stacking and Liquid Crystal Condensation of 6-to 20-Base Pair DNA Duplexes. *Science* **2007**, *318*, 1276–1279.
85. Bolhuis, P.; Frenkel, D. Tracing the Phase Boundaries of Hard Spherocylinders. *J. Chem. Phys.* **1997**, *106*, 666–687.
86. Frenkel, D. Onsager Spherocylinders Revisited. *J. Phys. Chem.* **1987**, *91*, 4912–4916.
87. Poniewierski, A.; Sluckin, T. J. Phase-Diagram for a System of Hard Spherocylinders. *Phys. Rev. A* **1991**, *43*, 6837–6842.
88. Onsager, L. The Effects of Shape on the Interaction of Colloidal Particles. *Ann. N. Y. Acad. Sci.* **1949**, *51*, 627–659.